CrossMark

Causes for the reversal of North Indian Ocean decadal sea level trend in recent two decades

U. Srinivasu[1] · M. Ravichandran[1,2] · Weiqing Han[3] · S. Sivareddy[1] · H. Rahman[1] · Yuanlong Li[3] · Shailesh Nayak[4]

Abstract Using satellite and in-situ observations, ocean reanalysis products and model simulations, we show a distinct reversal of the North Indian Ocean (NIO, north of 5°S) sea level decadal trend between 1993–2003 and 2004–3013, after the global mean sea level rise is removed. Sea level falls from 1993 to 2003 (Period I) but rises sharply from 2004 to 2013 (Period II). Steric height, which is dominated by thermosteric sea level of the upper 700 m, explains most of the observed reversal, including the spatial patterns of sea level change. The decadal change of surface turbulent heat flux acts in concert with the change of meridional heat transport at 5°S, with both being driven by decadal change of surface winds over the Indian Ocean, to cause sea level fall during Period I and rise during Period II. While the effect of surface net heat flux is consistent among various data sets, the uncertainty is larger for meridional heat transport, which shows both qualitative and quantitative differences amongst different reanalyses. The effect of the Indonesian Throughflow on heat content and thus thermosteric sea level is limited to the South Indian Ocean, and has little influence on the NIO. Our new results point to the importance of surface winds in causing decadal sea level change of the NIO.

1 Introduction

Sea level is an important indicator of climate change. Global mean sea level rise (SLR) is primarily contributed from ocean mass addition by melting of land-based ice and ocean thermal expansion caused by increased ocean heat content associated with anthropogenic warming. The rate of global mean SLR during the last two decades is 3.2 ± 0.4 mm/year (Nerem et al. 2010). Recent studies (Rignot et al. 2011), with the aid of satellite gravimetry, revealed an accelerated contribution from melting glaciers and ice caps and implied only about 1/3 of SLR contribution from thermal expansion. The rate of SLR, however, is not spatially uniform. It can be as high as three times the global mean in regions like western tropical Pacific (e.g., Merrifield 2011; Cazenave and Cozannet 2014; Han et al. 2014a) and can even be decreasing in some other areas like the southwestern tropical Indian Ocean (e.g., Han et al. 2010) and the eastern tropical Pacific (e.g., Merrifield 2011; Cazenave and Cozannet 2014; Han et al. 2014a). With the advent of satellite altimetry, it is possible for us not only to obtain an accurate estimate of global SLR but also to examine the spatial patterns of SLR, thus enabling us to assess regional sea level variability. In addition to thermal expansion, regional sea level variations largely depend on wind-driven circulation changes and therefore can be viewed as a superposition of global mean SLR and regional variability. While land ice melting increases sea level uniformly over the globe through adding mass into the ocean, its freshwater can impact ocean density

✉ M. Ravichandran
ravi@incois.gov.in

1 ESSO-Indian National Center for Ocean Information Services, Hyderabad 500090, India

2 ESSO-National Center for Antarctic and Ocean Research, Goa 403804, India

3 Department of Atmospheric and Oceanic Sciences, University of Colorado, Boulder, CO, USA

4 Earth System Science Organization (ESSO), Ministry of Earth Sciences, New Delhi 110003, India

and dynamics, and thus induce regional sea level change (Stammer and Hüttemann 2008; Stammer et al. 2011; Slangen and Lenaerts 2016). Additionally, due to gravitational effects and associated changes in shape and rotation of the Earth, changes in land ice mass input can also cause spatially uneven sea level change (e.g., Mitrovica et al. 2001). Existing literature, however, demonstrate that the observed regional patterns of decadal sea level variability (with global mean SLR removed) during the past few decades are primarily wind driven, with a large portion of the driving wind being associated with natural internal climate modes (see review articles by Stammer et al. 2013; Han et al. 2017). Regional sea level change is of immediate concern for understanding the impact of climate variability and change on coastal regions and low-lying areas (Milne et al. 2009; Church et al. 2011).

Studying sea level variability of the Indian Ocean is particularly important due to its economical and societal impacts on the vast inhabitant population of the region. It is especially devastating for low-lying coastal regions of river deltas in the Bay of Bengal, such as the Ganges Brahmaputra Delta, where SLR has a higher risk of destroying agricultural production through marine flooding (Cazenave and Cozannet 2014). Furthermore, under a rising sea level, storm surges associated with tropical cyclones lead to more severe destruction in the coastal areas of the Bay of Bengal especially Bangladesh and India (Karim and Mimura 2008). SLR can exacerbate the problem of seawater intrusion into the coastal aquifers (Bobba 2002; Werner and Simmons 2009) and thus reduce the quality of ground water. Aggravated coastal erosion and seawater inundation may force the large coastal population to be displaced to other regions (Rowley et al. 2007).

Several studies have investigated the regional sea level rise over the Indian Ocean. Cheng et al. (2008) suggested that sea level of Indo-Pacific Warm Pool sea level rises at a rate of 4.5 mm/year (6.0 mm/year in Western Pacific warm pool and 1.6 mm/year in Indian Ocean warm pool) over the 1993–2005 period, and that thermal steric change of the upper layer has a significant contribution. Timmermann et al. (2010) used a wind-forced simplified dynamical ocean model and showed that recent features of decadal and multidecadal sea level trends in the tropical Indo-Pacific can be attributed to changes in the prevailing wind regimes. Han et al. (2010) emphasized the importance of oceanic response to the forcing of changing winds. They showed a significant sea level decreasing trend in the southwest tropical Indian Ocean from 1961 to 2008, which rebounds during the last decade (their Fig. 2a). They attributed the observed trends of sea level for the 1961–2008 period to surface winds associated with enhanced Hadley and Walker circulation, which is likely partly associated with the warming of the Indian Ocean.

Overlying the multi-decadal trends, sea level over the Indian Ocean also exhibits basin-wide decadal variations (e.g., Lee 2004; Lee and McPhaden 2008). Ocean model experiments suggest that the observed basin-wide decadal sea level variation patterns result primarily from wind forcing over the Indian Ocean, with remote forcing from the Pacific via the Indonesian Throughflow (ITF) contributing most significantly in the eastern basin (Trenary and Han 2012; Nidheesh et al. 2013). Along the west coast of Australia, tide gauge and satellite altimeter data show large-amplitude decadal variability in sea level, which is strongly influenced by decadal variability in the western tropical Pacific via ITF (e.g., Feng 2004; Merrifield and Maltrud 2011), and the ITF effect has intensified since the 1990s (Trenary and Han 2012; Han et al. 2014a). Earlier reports suggested that thermal variations dominate decadal sea level variability during the 1966–2007 period (e.g., Nidheesh et al. 2013), and salinity contributions are significant only in a few areas [see Han et al. (2014b) for a review]. For instance, Llovel and Lee (2015) found large halosteric contribution to the 2005–2013 sea level trends in the southeast tropical Indian Ocean, and attributed it to the freshening of upper 300 m ocean.

Unlike global mean SLR, which is dominated by ocean mass addition (in recent decades), regional sea level variability is dictated by thermosteric changes (Cheng et al. 2008; Nidheesh et al. 2013), which are caused by either changes in the incoming surface net heat flux or spatial re-adjustments of the heat content due to changes in wind forcing patterns (Han et al. 2010; Timmermann et al. 2010). More recently, the sharp increase in the 700 m heat content (for the period 2003–2012) of the Indian Ocean has been attributed to enhanced heat advection from the Pacific through ITF (Lee et al. 2015). This study showed that although the heat uptake of the Pacific has increased sharply, the 700 m heat content of the Pacific has decreased. They showed that during this warming hiatus, 70% of the ocean heat gain now resides in the upper 700 m of the Indian Ocean. The recent studies of Lee et al. (2015), Vialard (2015) and Nieves et al. (2015) suggest that equatorial Pacific decadal wind variability (i.e. higher than usual rate of La Niña events during the last decade) associated with an increased heat transport to the Indian Ocean via the ITF is largely responsible for the increased heat storage in the Indian Ocean over the last decade. Trenary and Han (2012) pointed out that the influence from the Pacific on southern IO (SIO) decadal sea level change has increased since the 1990s. However, it will be interesting to know how the increased heat advection from the ITF redistributes over different parts of the IO.

Earlier studies focused on sea level changes of either the Indo-Pacific region or the South Indian Ocean or Indian Ocean as a whole. There are not many studies that explicitly

examine sea level variations in the North Indian Ocean (NIO), especially on decadal time scales. The heat balance mechanism of tropical Indian Ocean is unique as the northern boundary is located in the tropics and thus excessive heat over the NIO can only be transported southward. On the annual mean, the Indian Ocean wind structure is dominated by the summer monsoon. The southwesterly winds drive warm surface waters southward across the equator through Ekman transport. On an annual average, the NIO gains heat via net surface heat fluxes. This extra heat gain is transported across the equator to the SIO within surface branch of the wind-driven Cross-Equatorial Cell (CEC; Miyama et al. 2003; Lee 2004; Schott et al. 2004; Schoenefeldt and Schott 2006). While the surface branch of the CEC carries the warm surface water southward across the equator, the subsurface branch is associated with cold thermocline water that flows northward within the Somali Current, which upwells near the coasts of the NIO (Schott and McCreary 2001; Schott et al. 2009). The strength of winds not only affects the NIO surface turbulent heat flux but also the CEC strength and thus cross equatorial heat transport, which is crucial for maintaining the NIO heat balance.

Recently, Unnikrishnan et al. (2015) reported a SLR along the coasts of India during the last two decades (1993–2012) with a rate close to the global mean of 3.2 mm/year except for the northern and eastern Bay of Bengal, where the rate is 5 mm/year or larger. Here we find a distinct decadal reversal of sea level trend over the entire NIO basin near 2003, which overlies this multi-decadal SLR trend. To understand and delineate the effects of climate change on sea level of a region, it is essential to understand the underlying natural variability of the region. Here, we explore the causes for the observed decadal reversal of sea level (global mean SLR removed) over the NIO. Note that seismic activity can change geoid and therefore the absolute sea level, and the interpretation of ocean mass trends in the Indian Ocean using GRACE gravimetry data is ambiguous owing to the 2004 Sumatran–Andean earthquake (Quinn and Ponte 2010; Johnson and Chambers 2013). Furthermore, the crustal deformations and slow adjustment of continental crust (Post Glacial Rebound effect) can change relative sea level on long-term scales. Since sea level variations due to seismic activity are not significant (Melini and Piersanti 2006), the seismic effect is not examined in this study.

The rest of the paper is organized as follows. Section 2 describes the various datasets and methods used in this study. Section 3 reports and discusses the observed reversal of NIO decadal sea level trend during the 1993–2013 period, when sea level falls from 1993 to 2003 (Period I) but rises sharply from 2004 to 2013 (Period II). Section 4 explores the mechanisms behind this phenomenon. Finally, Sect. 5 provides a summary and discussion.

2 Data and methods

2.1 Sea level observations

Delayed-time monthly mean sea level anomaly (SLA) maps are obtained from the Archiving, Validation, and Interpretation of Satellite Oceanographic Data (AVISO) (Ducet et al. 2000) satellite altimeter data (ftp://ftp.aviso.altimetry. fr/global/delayed-time/grids/climatology/monthly_mean). They have a spatial resolution of ($1/4° \times 1/4°$) and extend from 1993 to the present. This is a merged product of several altimetry missions, namely TOPEX/Poseidon, Jason-1 and Jason-2, Envisat, ERS-1,2 and Saral/AltiKa. All geophysical corrections including removal of ocean tides and inverted barometer correction are applied. This product has been extensively used to understand the regional and global sea level variability at various time scales (e.g., Unnikrishnan et al. 2015; Cazenave and Cozannet 2014; Han et al. 2014a; Llovel and Lee 2015).

2.2 Gridded temperature and salinity products

Several temperature and salinity gridded products are used to estimate ocean heat content changes and steric contribution of the sea level in the Indian Ocean. These are monthly temperature and salinity fields (ISHII) available from 1945 at http://www.rda.ucar.edu/datasets/ds285.3 (Ishii et al. 2006), seasonal temperature and salinity fields from the World Ocean Atlas (WOA13; Levitus et al. 2012) since 1955, and monthly temperature and salinity fields from the ENACT/ENSEMBLES version 2a (EN4) database (Good et al. 2013) taken for the period 1993–2013. The data sources used to produce the most recent version of the EN4 dataset are World Ocean Database 2005 (WOD05), Global Temperature and Salinity Profile Programme (GTSPP), and Argo profiling floats and the Arctic Synoptic Basin-wide Observations (ASBO) project. Additionally, we use Roemmich-Gilson Argo Climatology (RGC) which is based on temperature and salinity profiles obtained only from Argo (Roemmich and Gilson 2009).

2.3 Reanlaysis and model simulation data

To investigate the changes in the ocean circulation and associated heat transports, we resort to two independent ocean reanalysis datasets: (1) ORAS4 and (2) NCEP-GODAS. ORAS4 reanalysis dataset (Balmaseda et al. 2013) is based on a variational data assimilation system called NEMOVAR (Mogensen et al. 2012) using version 3.0 of NEMO (Nucleus for European Modelling of the Ocean) (Madec 2015) as the ocean model. NEMOVAR assimilates temperature and salinity profiles, and along-track altimeter-derived sea level anomalies. The underlying

spatial grid of NEMO has a resolution of 1° in the extra-tropics and a finer resolution in the Tropics (0.3° meridional resolution near the equator). The model uses surface wind stress and other atmospheric fluxes derived from European Center for Medium Range Weather Forecasts (ECMWF) reanalysis system (ERA-Interim; Dee et al. 2011) as atmospheric forcing from 1989 to 2009. From 2010 on wards, daily surface-fluxes derived from the operational ECMWF atmospheric analysis are used to force the operational ORAS4. The ORAS4 ocean reanalysis product is available at 1° × 1° resolution. It is regarded as one of the best available ocean data assimilation products and has been successfully applied to various recent studies, including a recent study on the Indian Ocean equatorial undercurrent (Chen et al. 2015). In order to ascertain the quality of ORAS4 with regard to studying the circulation and heat transport, we have compared the currents from ORAS4 reanalysis with RAMA-ADCP data (McPhaden et al. 2009) at several moorings locations during period II. Currents from ORAS4 reasonably represent the vertical structure and magnitude of the meridional currents across the equator (Figures not shown). The mean RMSE of the meridional current (in the upper 150 m) of ORAS4 with respect to two RAMA ADCP locations (at 80.5°E and 90°E at Equator) is 6.12 cm/s during the period (2004–2013) which is better than that of NCEP-GODAS (7.39 cm/s) and HYCOM (7.52 cm/s) which are described below. The surface meridional currents for the same period are equally good for ORAS4 (r=0.55) compared to NCEP-GODAS (r=0.19) and HYCOM (r=0.28), since the correlation coefficient (r) is better between ORAS4 and RAMA, compared to others.

The other ocean re-analysis product used in this study is NCEP-GODAS (National Centers for Environmental Prediction-Global Ocean Data Assimilation System). The NCEP-GODAS is based on GFDL-MOMv3 and uses 3DVAR assimilation scheme (Behringer and Xue 2004). The model domain extends from 75°S to 65°N and has a resolution of 1°×1° enhanced to 1/3° within 10°S–10°N. The momentum, heat and fresh water fluxes for the model are taken from NCEP atmospheric Reanalysis 2 (Kanamitsu et al. 2002). NCEP-GODAS assimilates temperature and synthetic salinity profiles.

The SST of both NCEP-GODAS and ORAS4 are relaxed toward observations. Differences between the two re-analyses, particularly the velocity fields, could be due to the differences in the approaches of assimilating observations. ORAS4 assimilates temperature and salinity profiles as well as the sea surface height anomaly, whereas NCEP-GODAS assimilates only the observed temperature and synthetic salinity profiles and does not assimilate sea surface height. Also, the assimilation approach of ORAS4 incorporates the linear long-term trend in observed sea level by providing appropriate corrections to freshwater forcing. They consider salinity corrections along isopycnals while preparing salinity analysis. The temperature, salinity and SSH increments influence the velocity fields by means of geostrophic balance, which is imposed using a beta-plane formulation near the equator. These additions, which are missing in NCEP-GODAS, improve ocean state significantly (Balmaseda et al. 2013; Vidard et al. 2009). Another important factor that may have contributed to the differences, is the use of synthetic (artificial) salinity for assimilation in NCEP-GODAS, while ORAS4 assimilates observed salinity profiles.

Apart from the reanalysis products, a forced (with no data assimilation) ocean simulation based on the HYbrid Coordinate Ocean Model (HYCOM) has been analyzed. For this simulation, HYCOM version 2.2.8 has been configured to the Indian Ocean Basin (30°E–122.5°E, 50°–30°) with a horizontal resolution of 0.25°×0.25° (Li and Han 2015). The atmospheric surface forcing fields are taken from NCEP/NCAR (National Center for Atmospheric Research) Reanalysis data. This model configuration excludes the remote forcing effect from the Pacific Ocean through ITF variability. At the western, eastern, and southern open-ocean boundaries 5° sponge layers are applied to relax model temperature and salinity to WOA09 monthly climatology. The sponge layer on the eastern boundary considers the mean temperature and salinity properties of the ITF. This simulation helps to delineate the effects of ITF on Indian Ocean variability. We refer to this simulation as HYCOM.

2.4 Surface heat flux products

Various surface heat flux products are analyzed to study their effect on the observed heating of the NIO. These are the Tropflux (Praveen Kumar et al. 2012) data from http://www.incois.gov.in/tropflux/, National Oceanographic Center's Surface (NOCS) version 2.0 flux (Berry and Kent 2011) from Computational and Information Systems Laboratory (CISL), OAFlux (Yu and Weller 2007) from http://oaflux.whoi.edu/heatflux.html, ERA-Interim (Dee et al. 2011) and NCEP2 (Kanamitsu et al. 2002) heat fluxes from Asia-Pacific Data-Research Center (APDRC). Additionally, surface heat fluxes from twentieth century reanalysis (Compo et al. 2011) are used as an independent product to confirm the results. The twentieth century reanalysis (20 cra) assimilates only surface pressure data and uses observed monthly sea surface temperature and sea ice distributions as boundary conditions. To calculate the strengths of wind speed, Subtropical Cell and Cross Equatorial Cell (see Sect. 4.1 for description), wind data from ERA-Interim, NCAR/NCEP2 reanalysis and multi-satellite Cross-Calibrated Multi-Platform (CCMP; available at http://rda.ucar.edu/datasets/ds745.1/#!access) Ocean

Surface Wind Vector Analyses (Atlas et al. 2009) are used. Additionally, winds from Japanese 55-year Reanalysis (JRA-55) (Ebita et al. 2011) from http://rda.ucar.edu/data-sets/ds625.0 are used to study the longer-term changes of wind driven circulations.

In order to accentuate regional patterns in sea level i.e., the decadal reversal of sea level trend over the NIO region, the global mean SLR has been removed from the sea level data over the Indian Ocean basin. The percentages of confidence intervals of linear trends are computed based on the methods described in Santer et al. (2000). In this method, the test statistic (t_b equals to the ratio of estimated error of trend and its standard deviation) is assumed to be distributed as Student's t. The computed t_b is then compared with a critical value of t for a given significance level and number of degrees of freedom (n-2; n being the number of data points in the time series). The statistical significance of correlations is estimated using Student's t test (Devore et al. 2014). Steric sea level is calculated by integrating specific volume anomaly down to 700 m depth. The surface heat fluxes have been spatially integrated over the NIO to yield the units of Petawatt (PW) to compare them with cross-equatorial heat transports. The NIO is appropriately masked to exclude South China Sea using a high-resolution mask.

3 Observed decadal change of NIO sea level

Figure 1 shows the time series of monthly-mean sea level variations averaged over the Indian Ocean (IO; 30°E–120°E, 30°S–30°N) and the NIO (30°E–120°E, 5°S–30°N) with global mean SLR retained (Fig. 1a, b) and removed (Fig. 1c, d), the Arabian Sea (AS; 50°E–78°E, 8°N–26°N) and the Bay of Bengal (BOB; 77°E–103°E, 5°N–23°N) with global mean SLR removed (Fig. 1e, f) from 1993 to 2013. The linear trends for 1993–2003 (Period I) and 2004–2013 (Period II) are also plotted in Fig. 1 for each region. Evidently, over the Indian Ocean, particularly over the NIO, SLR has accelerated during Period II with respect to Period I (Fig. 1a, b). While they have comparable rising rates of 5.58±0.23 and 6.11±0.26 mm/year for Period II, the NIO essentially has no SLR during Period I (−0.37±0.26 mm/year) and the Indian Ocean has a slower rising rate of 1.89±0.22 mm/year (Fig. 1a, b). After the global mean SLR is removed, sea level anomalies averaged over different regions of the Indian Ocean basin exhibit consistent decadal changes near 2003, falling from 1993 to 2003 and rising from 2004 to 2013 (Fig. 1c, f). This decadal reversal is most apparent over the NIO, the Arabian Sea and the BOB. This reversal seems to have occurred a little earlier in the AS. In the NIO, sea level decreases at the rate of −3.27±0.26 mm/year during Period I, which

essentially balances the global mean SLR, but increases at the rate of 3.21±0.26 mm/year faster than the global SLR during period II. The fastest SLR occurs in the BOB in the past decade, with a rising rate of 3.93±0.73 mm/year above the global SLR from 2004 to 2013. Together with the global SLR, the BOB-mean sea level has increased by ~7 cm in the past decade. In contrast, sea level in the Arabian Sea falls by −4.34±0.49 mm/year during period I, which completely overcomes the global SLR, and its SLR during period II is 2.56±0.44 mm/year faster than the global SLR (Fig. 1e). Consequently, the Arabian Sea shows the strongest reversal (compared to BOB, NIO and IO) of sea level change relative to global mean SLR. Sea level fall in the western Indian Ocean during period I was reported in earlier studies (Cheng et al. 2008; Church et al. 2011).

To reveal the spatial pattern of basin-wide decadal sea level change, we perform a linear trend analysis over the global ocean with global mean SLR removed (Fig. 2). Consistent with the above analysis, over the Indian Ocean basin north of 5°S sea level exhibits basin-wide falling from 1993 to 2003 and rising from 2004 to 2013 relative to the global mean SLR (Fig. 2a, b, see the boxed areas), albeit with spatial differences in magnitudes. For example, sea level fall during period I is largest in the western basin. South of 5°S, however, no appreciable decadal reversal is observed. The sea level fall in the tropical southwest Indian Ocean and rise for the rest of the South IO appear in both period I and period II, a pattern that is consistent with that of the longer-term trend (Han et al. 2010). Interestingly, this basin-wide decadal reversal of sea level trend has not occurred in either the tropical Pacific or Atlantic (Fig. 2), even though SLR in the western tropical Pacific has been intensified during recent decades (Han et al. 2014a). This basin-scale sea level reversal is well captured by the upper 700 m steric sea level (Fig. 2c-d), albeit with quantitative differences in some areas. With global mean steric SLR retained, total steric (from EN4) explains 60% of the total sea level trend, whereas thermosteric sea level explains 74% of the trend, suggesting that halosteric sea level compensates for thermosteric sea level as a result of wind-driven advection (Stammer et al. 2013). The linear trend of steric SLR averaged over the NIO (with global mean steric SLR removed) is 3.09 mm/year for Period II, which explains approximately 94% of the observed total NIO SLR. This result shows the dominance of steric effects over mass on the observed NIO SLR. Residues are computed by taking the difference between AVISO sea level and thermosteric sea level (global mean SLR removed) for all the observational products and ORAS4 data. The mean residue for Period II from the observational products (EN4, ISHII, WOA and RGC) is only 0.36 mm/year, further demonstrating that the observed sharp SLR over the NIO in the past decade results from thermal expansion rather than from mass gain.
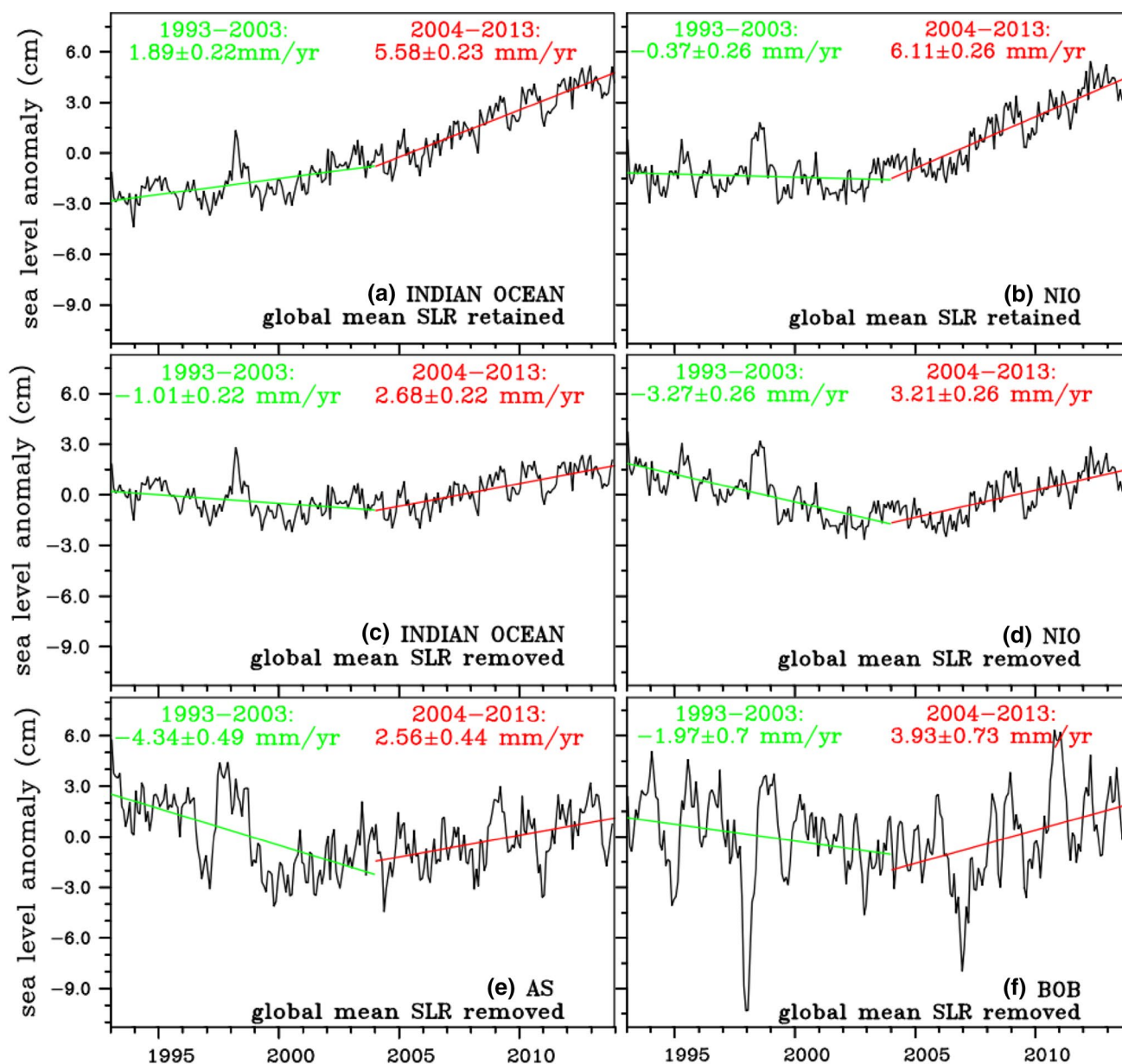
Fig. 1 Time series of monthly-mean sea level anomalies (SLA) from satellite altimeter data for 1993–2013. Linear trends for Period I (1993–2003; *green*) and Period II (2004–2013; *red*) are also plotted with their magnitudes each exceeding 99% significance. **a** SLA averaged over the Indian Ocean (IO; 30°E–120°E, 30°S–30°N), including global mean sea level rise (SLR); **b** SLA averaged over the North Indian Ocean (NIO; 30°E–120°E, 5°S–30°N), including global mean SLR; see Fig. 2 for justification of choosing 5°S as its southern bound; **c** Same as **a** but excluding global mean SLR; **d** Same as **b** but excluding global mean SLR; **e** SLA averaged over the Arabian Sea (AS; 50°E–78°E, 8°N–26°N), excluding global mean SLR; **f** SLA averaged over the Bay of Bengal (BOB; 77°E–103°E, 5°N–23°N), excluding global mean SLR

Sea level fall during Period I and rise during Period II are well reproduced by thermosteric time series from all observational products and ORAS4 reanalysis (Fig. 3). Time series of the annual mean upper 700 m EN4 thermosteric sea level averaged over the NIO (with linear trend of 1993–2013 removed) correlates well with the satellite observed AVISO sea level, with a correlation coefficient of 0.77 for the 1993–2013 period (black and purple curves of Fig. 3). The annual mean upper 700 m thermosteric sea level from Ishii et al. (2006) data also agrees reasonably well with the AVISO sea level for their overlapping period of 1993–2013 (red and purple curves of Fig. 3), with a correlation coefficient of 0.70 comparing to the coefficient of 0.46 for AVISO/WOA13 and 0.47 for AVISO/ORAS4 (Fig. 3), with all exceeding 99% significance. The upper 2000 m thermosteric sea level from EN4 data displays
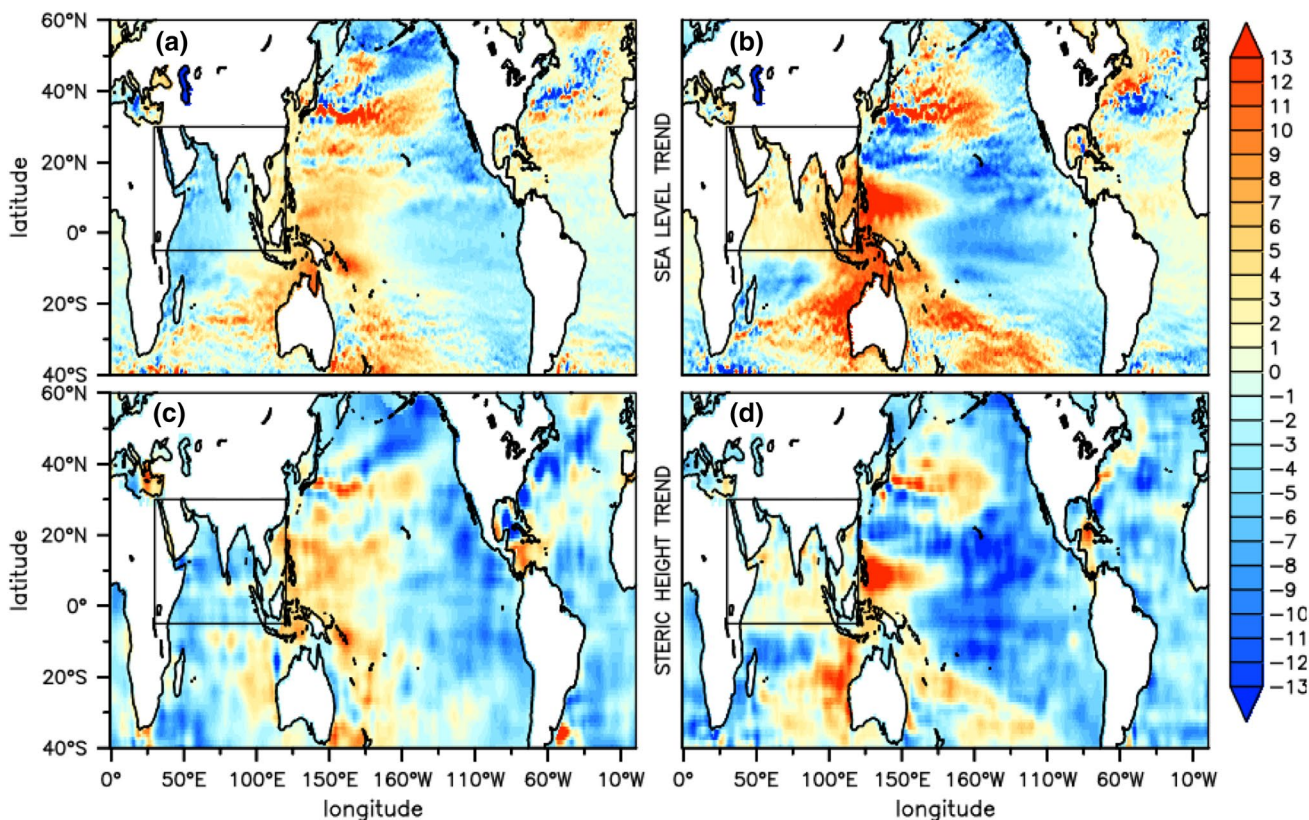
Fig. 2 Satellite observed spatial pattern of sea level trend (with global mean SLR removed) from AVISO data for the period of **a** 1993–2003 (Period I), and **b** 2004–2013 (Period II); **c** and **d** are the same as **a** and **b**, respectively, except for 0–700 m steric (thermal + halo) sea level trends from EN4 data. The *rectangular box* in each *panel* shows the region of decadal reversal of sea level, which is north of 5°S

comparable correlation of 0.69 with AVISO data, while the total steric height displays somewhat lower correlation (0.60 for 700 m and 0.53 for 2000 m). The inadequate resolution and errors in salinity field, together with the under sampling of the 700–2000 m comparing to the upper 700 m ocean, may account for the lower correlations in the total steric sea level compared to the thermosteric sea level.

Evidently, the observed decadal reversal of sea level over the NIO, including the rapid sea level increase in the past decade, is part of the decadal-scale variability over a longer-period data record (Fig. 3). In general, the yearly Ishii et al. (2006) and WOA13 thermosteric sea level data agree, with a correlation coefficient of 0.63 (>99% significance) from 1955 to 2013, while ORAS4 sea level displays poor correlation of 0.38 with Ishii and 0.40 with WOA13. Significant differences, however, occur in WOA13 data in the late 1990s and early 2000s, when WOA13 apparently deviates from AVISO, Ishii and EN4 data. A decreasing and increasing trend similar to that of last two decades can be observed for the period ~1963–1983 from the average of EN4, Ishii and WOA thermosteric time series (Fig. 3 dashed cyan), although the change is not as sharp as the

most recent reversal. During our period of interest from 1993 to 2013, the 5-year running mean ORAS4 reanalysis sea level data generally agrees with AVISO data, with both showing sharp decadal reversal of sea level change from period I to period II after the global mean SLR removed. This point will be further discussed in Sect. 4.1 below.

4 Causes for the decadal change of NIO sea level

Since the decadal change of sea level over the NIO has a basin scale (Fig. 2), we examine the causes for sea level change over the NIO as a whole, which is essentially a semi-closed basin with only one opening to the south near 5°S. Thus, the possible effect of direct advective heating by ITF on NIO sea level is avoided, since the ITF is primarily located between 8°S and 12°S (Sprintall et al. 2009). Note that similar reversals in SLR are obtained when we choose the southern boundary of NIO at the Equator or at 10°S (figures not shown). In the semi-enclosed NIO basin, sea level change can be caused by (1) ocean mass and heat transport across 5°S, (2) thermal expansion/contraction due
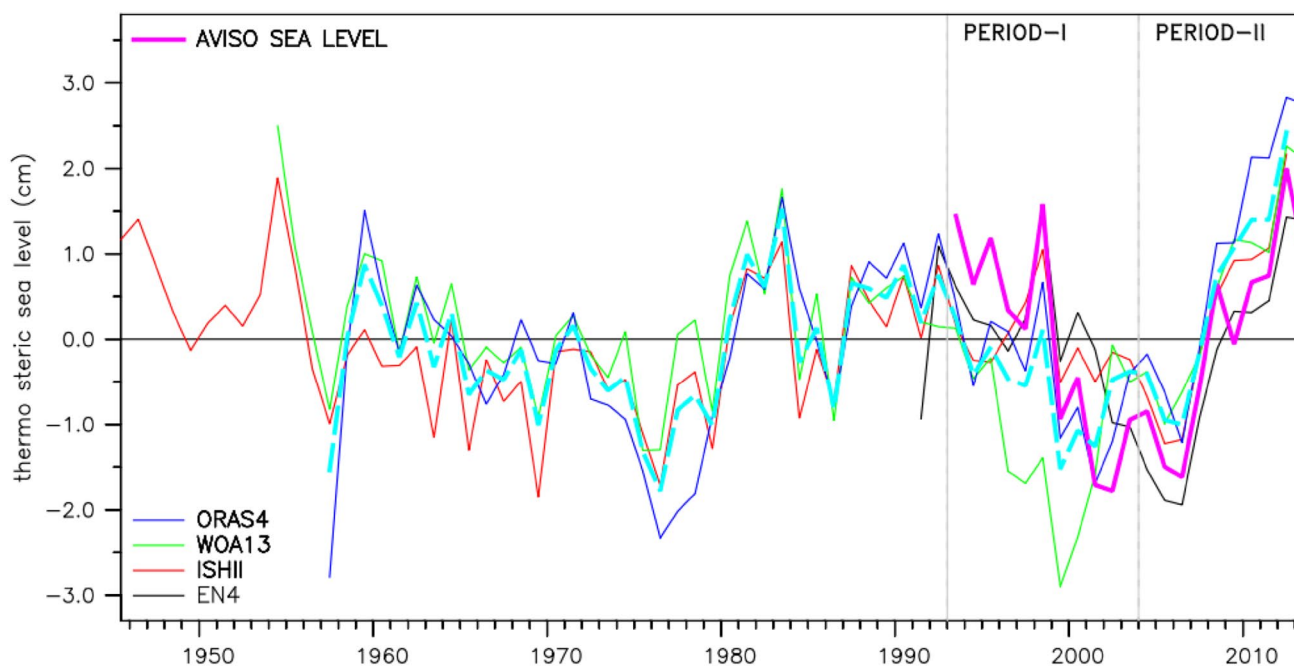
Fig. 3 Time series of annual mean 0–700 m thermosteric sea level averaged over the NIO from WOA13 from 1955 to 2013 (*green*), ISHII for 1945–2013 (*red*) and EN4 for 1993–2013 (*black*) together with the thermosteric sea level of ORAS4 reanalysis for 1958–2013 (*blue*) and satellite observed sea level (*purple*) for 1993–2013; the average of WOA13, ISHII and EN4 thermosteric sea level time series is plotted over (*cyan dashed*). Linear trend for each dataset record is removed. Periods I and II are demarcated with *vertical gray lines*

to surface heating/cooling and (3) halosteric changes due to evaporation, precipitation, river discharge and lateral salinity transport across 5°S. Figure 3 shows good agreement between the thermosteric sea level (WOA13, ISHII and EN4) and total sea level (AVISO and ORAS4) trends for both Period I and period II, demonstrating that (3) is weak, i.e. surface heat flux and heat transport across 5°S play dominant roles in determining the NIO decadal sea level reversal. The halosteric component compensates for the thermal steric sea level rise during Period II, consistent with Stammer et al. (2013), but has no apparent trend during Period I. This is further demonstrated by Fig. 4, which shows that the halosteric component plays no role in the trend reversal for two distinct data-sets (EN4 and RGC). In this study, we considered heat transports computed up to 700 m depth. In principle, transport through the bottom of the box (i.e. 700 m) can also play a role. This is quite unlikely because, given the weak gradients at that depth, the vertical velocity or mixing would have to be unrealistically high for that term to play a role.

Given the dominance of upper 700 m thermosteric sea level (Figs. 2, 3), we examine the heat budget equation integrated over upper 700 m of the NIO, as given by Eq. (1a) below, which shows that the NIO heat storage is primarily determined by net surface heat flux (*Qnet*) and heat transport across 5°S (*Qtr*).

$$\frac{\partial HC_t}{\partial t} = \int_S^N \int_W^E Q_{net} dx dy + \int_W^E Q_{tr} dx + Rs \qquad (1a)$$

where N, S, E and W are the respective Northern (30°), Southern (−5°), Eastern (120°) and Western (30°) boundaries of the NIO. HC_t is the spatially integrated heat content of the domain, $Qnet$ is the surface net heat flux (W/m²), Qtr is heat transport across 5°S, and Rs is the residual term which includes the effects of unresolved eddy heat transport, heat transport from below 700 m, mixing, diffusion and calculation errors. For HYCOM simulation and data assimilation products, model and forcing errors and non-physical assimilation increments can also contribute to this residual error. Heat content and Qtr are computed down to depth of 700 m.

Given that the 5-year running mean sea level of reanalysis products (ORAS4 and NCEP-GODAS) agree reasonably with AVISO data for our period of interest (Fig. 5), and ORAS4 currents along the equator agree with RAMA currents (that are not assimilated into the ORAS4 product, see Sect. 2), here we use the current and temperature of the reanalysis to calculate the oceanic meridional heat transport into/out of the NIO. In general, currents from the data assimilation systems are known to have degraded quality when other variables are assimilated (e.g., Ravichandran et al. 2013). It is worth noting that NCEP-GODAS velocity

Fig. 4 Halosteric sea level component compared with AVISO SLR averaged over the NIO. *Black line* shows the AVISO SLR, *red line* shows the halosteric component computed from EN4 data and *green line* shows the same computed with Roemmich-Gilson Climatology (RGC) Argo data. Linear trends for Period II are plotted over in the respective *colors*
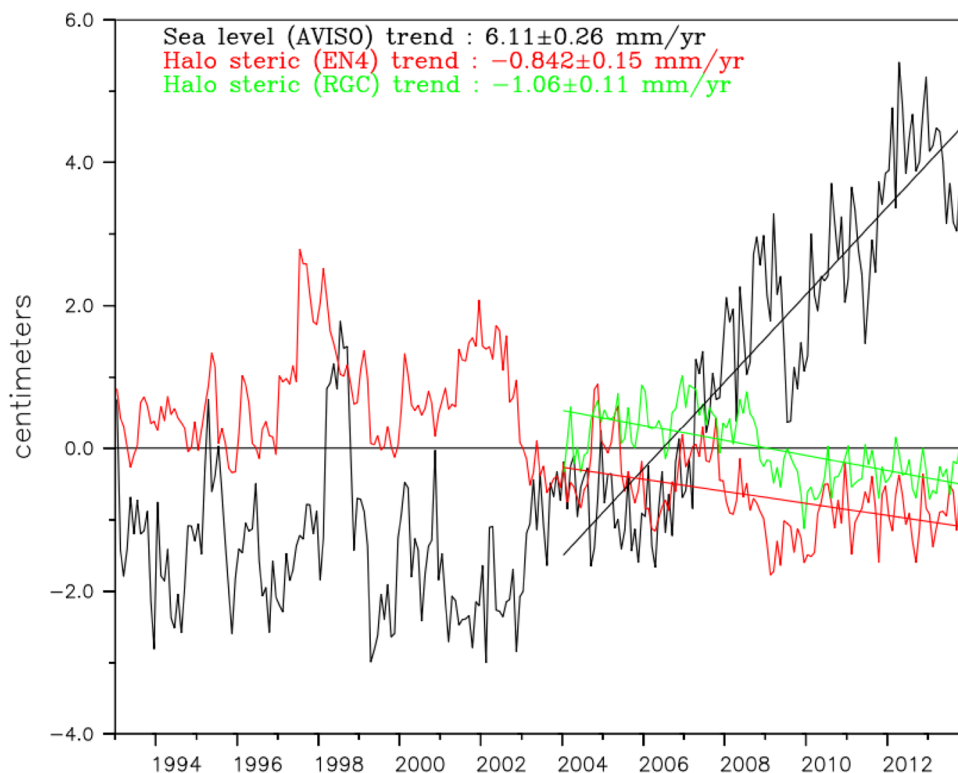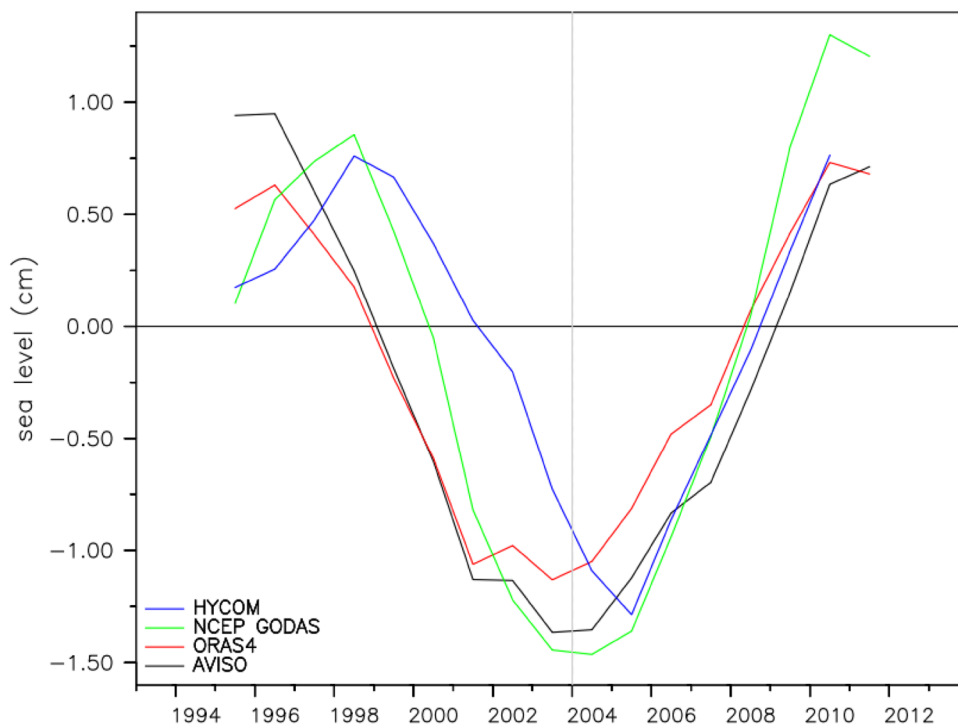

Fig. 5 Time series of 5 year running mean of sea level averaged over the NIO (north of 5°S) with the linear trend of 1993–2013 removed for AVISO satellite data (*black*), HYCOM (*blue*), NCEP-GODAS (*green*) and ORAS4 data (*red*)

fields are unreliable owing to the poor correlation of meridional currents with the RAMA currents in the Equatorial Indian Ocean (figures not shown). Inter-comparison between INCOIS-GODAS, ORAS4 and NCEP-GODAS conducted by Sivareddy ([2015](#)) has already indicated that NCEP-GODAS suffers from poor representation of ocean state especially salinity and currents. To further verify their results in the context of the present study, we have

performed preliminary validation of NCEP-GODAS and ORAS4 with RAMA and Argo, which shows that ORAS4 data have more accurate temperature and velocity fields than NCEP-GODAS data (not shown).

It is striking to observe a similar reversal in sea level trends with a forced ocean model, HYCOM which has no data assimilation and excludes the ITF. As shown in Fig. 5, the observed NIO sea level fall during Period I and rise during Period II are well simulated by HYCOM even though the reversal seems to occur one and half years later than other datasets. The spatial pattern of steric height is also well reproduced by HYCOM, similar to observations shown in Fig. 2c, d (figure not shown). Since HYCOM has no ITF influence, this result clearly demonstrates that the NIO sea level reversal results primarily from a variation of the circulation within the Indian Ocean rather than from exchanges with the Pacific through the ITF. To further verify this result, we analyze the detrended heat content anomaly in the NIO and SIO (30°E–120°E, 30°S–5°S) for Period I and Period II (Table 1). All models and observations exhibit a decline in heat content for both the NIO and SIO regions during Period I. During Period II, heat content of the NIO has increased in both reanalysis data and in HYCOM, with anomalies being 0.69×10^{22} J in EN4, 0.81×10^{22} J in NCEP-GODAS, 0.71×10^{22} J in ORAS4 and 0.56×10^{22} J in HYCOM. Heat content anomalies in the SIO do not agree being -0.16×10^{22} J, 0.63×10^{22} J, 0.13×10^{22} J and -0.72×10^{22} J respectively for the above datasets. The larger decline in the SIO heat content in HYCOM simulation comparing with reanalysis data may result partly from the lack of heat advection from the Pacific through ITF, which is excluded from HYCOM. These results indicate that heat advection from ITF may contribute to the SIO heat content change but it has little influence on the NIO. It is worth mentioning here that the

temperature field of HYCOM is not as good as ORAS4, since it does not assimilate any temperature data (figures not shown). Thus, heat transport results from HYCOM are not as reliable as ORAS4. For this reason, our discussions below are mainly based on ORAS4 dataset, since it is better than other reanalysis products and HYCOM simulation.

4.1 Heat budget analysis of ORAS4 reanalysis associated with the decadal reversal

In this section, we first present the heat budget analysis using the ORAS4 data to explain the reversal of decadal sea level trend. Then, we examine the robustness of our results by analyzing surface heat fluxes and heat transports across 5°S from other reanalysis products. As described in Sect. 2, ORAS4 reanalysis is forced by ERA-Interim wind-stresses and radiative fluxes during our period of interest (1993 onward). Figure 6a shows the spatially integrated surface net heat flux of ERA-Interim and zonally integrated (between 30°E and 120°E) 700 m heat transport at 5°S. A clear reversal of both surface-fluxes and heat transport can be noticed to occur around the year 2000 (4 years prior to the actual reversal of sea level). For the period 1993–2003, heat transport across 5°S has a negative (southward) anomaly (Fig. 6a, solid red curve), changing from a northward value of 0.037 PW near 1996 to a southward value of −0.045 PW near 2000. This result demonstrates that more heat was transported out of the NIO during Period I (−0.247 PW; the mean transport for the Period-I) compared to the climatological mean (−0.180 PW), which contributed to the NIO sea level fall observed from 1993 to 2003 (Fig. 5, red). By contrast, from 2004 to 2013, less heat (−0.106 PW) was transported out of the NIO, thereby increasing heat content in the NIO, thus contributing to the observed sea level rise. The averaged heat transport anomaly is southward for Period I and northward for period II, supporting a mean sea level reduction for period I and increase for Period II. The maximum extent (peak to peak variation) of heat transport change between 2000 and 2010 is approximately 0.12 PW. This is similar to the maximum extent of the net surface heat flux change of ~0.15 PW from ERA-Interim data (black curve of Fig. 6a, the forcing of ORAS4), but with some phase differences. These results suggest that net surface heat flux and meridional heat transport have comparable contributions to the NIO sea level reversal.

Heat budget analysis for the NIO heat content (HC) in the upper 700 m using ORAS4 data based on Eq. 1a further confirms above results. The HC tendency $\frac{\partial HC_t}{\partial t}$ (black solid line in Fig. 6b) is highly correlated with heat transport (green line), with correlation coefficient of 0.77. The correlation with surface net heat fluxes (red line) is significantly lower with correlation coefficients of −0.13. This result shows that interannual variability of the HC tendency is

Table 1 Changes in the heat content values from the time series of detrended heat content anomaly (10^{22} J) for Period I (1993–2003) and Period II (2004–2013) for the northern and southern parts of the Indian Ocean computed from observational product, reanalyses and HYCOM simulation

	NIO: 30°E–120°E, 5°S–30°N		SIO: 30°E–120°E, 30°S–5S°	
	1993–2003	2004–2013	1993–2003	2004–2013
EN4	−0.2663	0.6978	−0.0320	−0.1617
NCEP-GODAS	−0.3823	0.8158	−0.2332	0.6319
ORAS4	−0.8347	0.7112	−0.6069	0.1265
HYCOM	−0.2814	0.5605	−0.2612	−0.7277
RGC		0.1333		0.3229
WOA	−0.4058	0.3568	−0.4081	−0.2332
ISHII	−0.2059	0.6464	−0.7140	0.1268

Note that RGC data is available only for the Period II

Fig. 6 a Five year running mean of time series of heat transport at 5°S using ORAS4 data (*red*) and ERA-Interim surface net heat flux (*black*); **b** Terms of NIO heat budget equation (see Eq. 1a) shown by: *black solid* (heat content change or heat storage, dHC/dt term), *red* (Qnet term), *green* (Qtr term) and *blue dashed* (Qnet + Qtr term); **c** values of time integrated heat budget terms for Period I and Period II (*green* Qnet; *blue* Qtr and *cyan* Qsum) compared with the heat content differences (in 10^{22} J) for the beginning and end of each period (*black bars*) and equivalent 700 m heat content required to raise the thermosteric level to the observed values (*red bars*) for Periods I and II
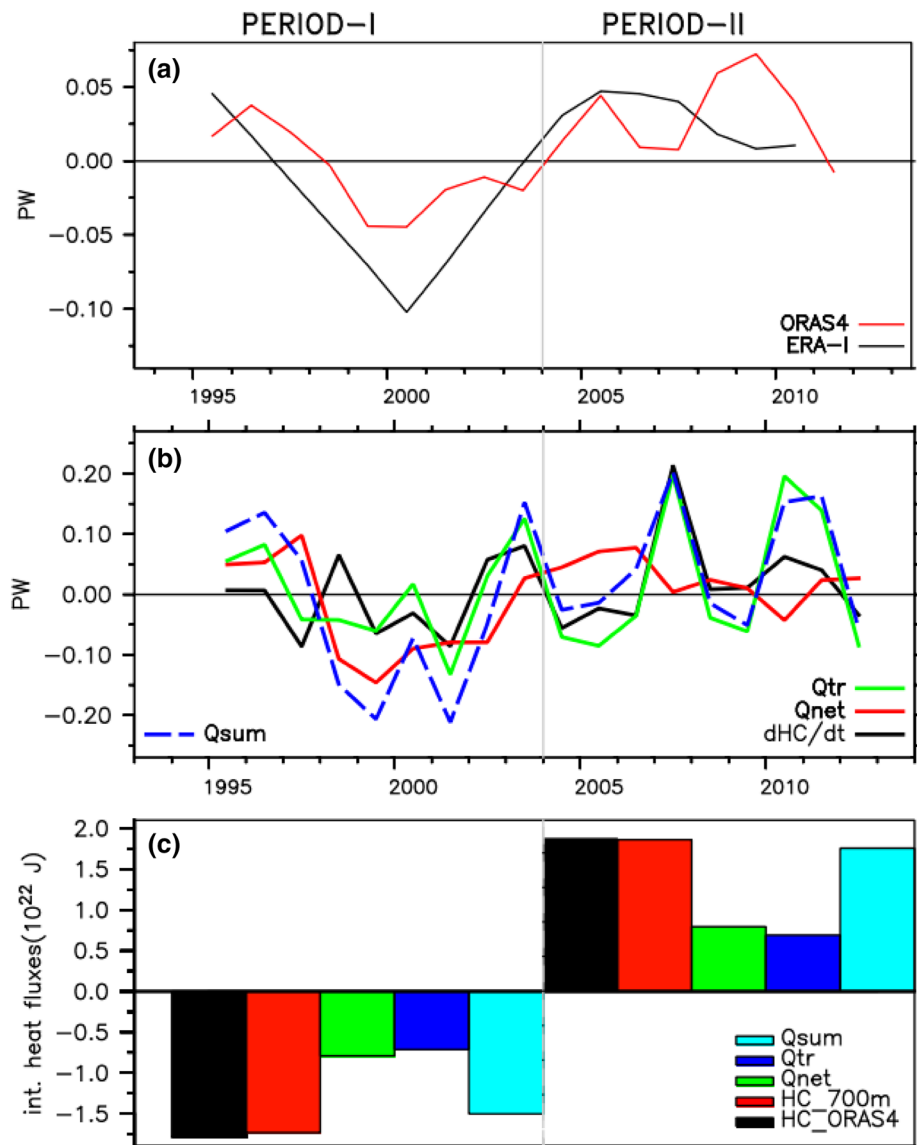
more dominated by heat transport. When we integrate each term over Period I and Period II (see Eq. 1b below), however, the effects of surface heat flux and heat transport at 5 S are comparable (green and blue bars of Fig. 6c).

$$HC_t = HC(0) + \int_0^t \int_S^N \int_W^E Q_{net} dx dy dt + \int_0^t \int_W^E Q_{tr} dx dt + Rs'.$$
(1b)

Specifically it can written for Period II as

$$HC(t = 2013) - HC(t = 2004) = \int_{2014}^{2013} \int_S^N \int_W^E Q_{net} dx dy dt$$
$$+ \int_{2004}^{2013} \int_W^E Q_{tr} dx dt + Rs'.$$
(1c)

For ORAS4 data, Qsum integrated in time for Period II is 1.48×10^{22} J, with 0.69×10^{22} J contributed from heat transport anomaly (47%) and 0.79×10^{22} J (53%) from surface net heat flux anomaly (Fig. 6c). The Qsum integrated for Period II (Period I) is roughly equal to the difference of NIO heat content between the end and beginning of the Period II (Period I). This balances Eq. 1c. The heat content change required (equivalent heat content) to change the thermosteric sea level to the observed quantities is plotted as red bars for the respective periods, which are almost equal to the heat content differences (black bars). These results further demonstrate that, in ORAS4, changes in surface heat flux and meridional heat transport contribute roughly equal to the observed NIO decadal sea

level reversal, through their impact on thermosteric sea level.

Note that Qsum (Qnet + Qtr) is not exactly equal to dHC/dt (Fig. 6b) and thus Rs' term in Eq. 1b is not zero. Possible reasons for the errors are that the budget analysis is made "offline" using monthly data, instead of doing the budget calculation for every step in the model during the model integration. This can cause large calculation errors. Moreover, using "monthly mean" data significantly underestimate the "eddy heat transport" (and none of the models used are eddy resolving) and heat transport variability induced by synoptic and intraseasonal oscillations. As discussed above, mixing and diffusion will also contribute to the errors.

4.2 Robustness of signals across different datasets

Figure 7a shows surface net heat flux spatially-integrated over the NIO region computed from several products. At the ocean surface, the net heat flux trend is negative during 1993–2001 and positive after 2001, indicating that the ocean lost heat to the atmosphere during Period I but gained heat during period II. It is evident that there is a phase lag of ~3–4 years between surface net heat flux and sea level changes. There is clear and coherent consensus among different products in representing the significant change in net heat flux anomalies, except that NCEP2 shows a larger variation during Period II. This coherence is more evident in time-integrated net heat fluxes during each period for different products (Fig. 7b). The decadal reversal of net surface heat flux anomaly results primarily from
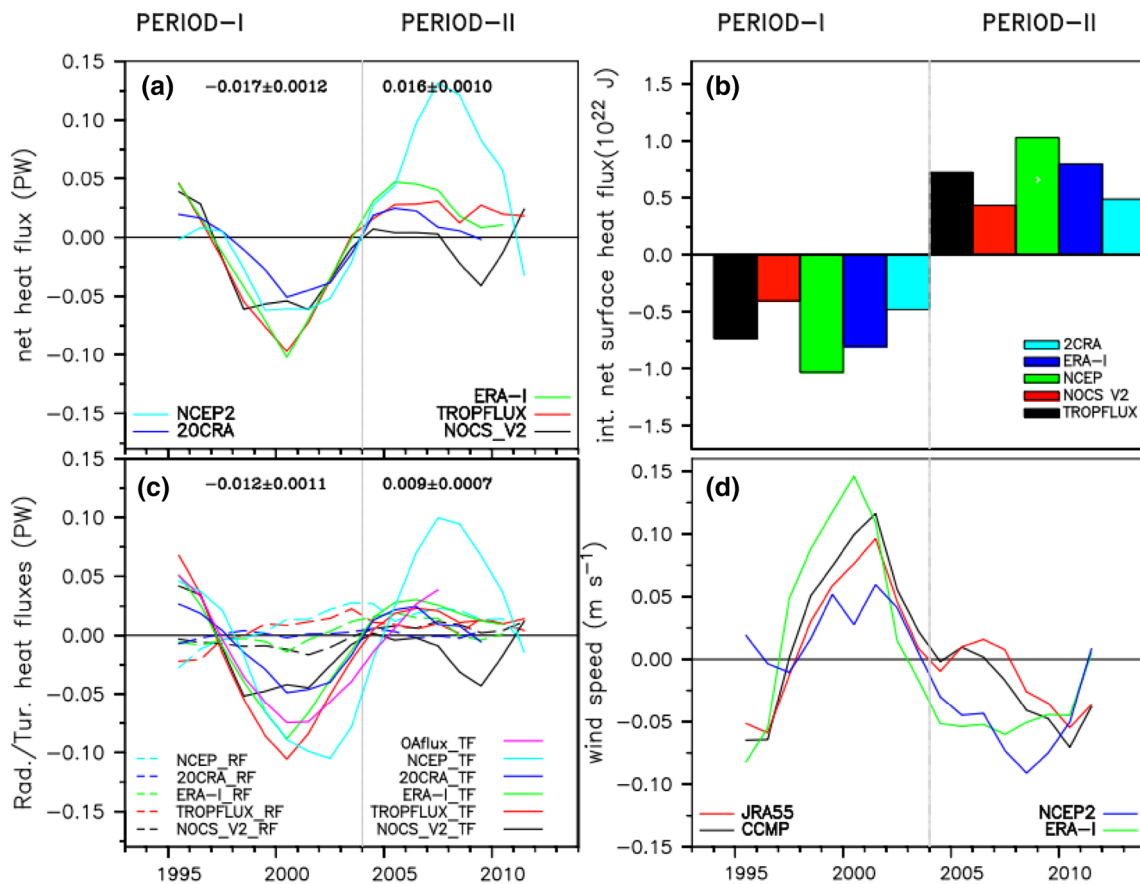
Fig. 7 **a** Time series of 5-year running averages of net surface heat flux integrated over the NIO (north of 5°S) with linear trend of 1993–2013 removed from NCEP2 (*cyan*), twentieth century reanalysis (*blue*), ERA-Interim (*green*), Tropflux (*red*) and NOCS_V2 (*black*) data; **b** time integrated surface net heat fluxes (in 10^{22} J) for Period I and Period II, plotted as *bars* having the same colors as that of **a**, **c** time series of 5 year running averages of net radiative flux (SW + LW; *dashed*) versus turbulent heat flux (Qsen + Qlat; *solid*) integrated over the NIO with linear trend for 1993–2013 removed from NCEP2

(*cyan*), twentieth century reanalysis (*blue*), ERA-Interim (*green*), Tropflux (*red*) and NOCS_V2 (*black*); turbulent heat flux obtained from OAFlux (*solid purple*) is also added to this figure; **d** time series of 5 year running mean surface wind speed averaged over the NIO with linear trend of 1993–2013 removed from JRA55 (*red*), multiple satellite CCMP winds (*black*), NCEP2 (*blue*) and ERA-Interim (*green*). The mean values of the variables for the Periods I and II are indicated at the *top* of the panels **a**, **b** and for **b**, those values correspond to the means of turbulent heat fluxes

turbulent (sensible + latent) heat flux forcing, with radiative (short wave + long wave) flux having negligible contributions (Fig. 7c). The basin-wide enhancement of surface wind strength over the NIO from 1993 to 2001 (Fig. 7d) increases evaporation, causing surface heat loss via turbulent heat flux and thus decreasing thermosteric sea level. By contrast, the basin-wide weakening of surface wind strength over the NIO for 2001–2013 (Fig. 7d) reduces evaporation and thus turbulent heat loss, causing surface heat gain and therefore increasing thermosteric sea level.

Compared to the surface heat fluxes, meridional heat transports calculated from different reanalysis products and HYCOM simulations are less consistent (Fig. 8). Even though, the heat transports of both the NCEP and HYCOM display decreasing trend during Period I and increasing trend during Period II (green and blue curves of Fig. 8a), which agree with ORAS4 data (red), the time integrated transports from NCEP have opposite signs with ORAS4 and HYCOM (Fig. 8b). This is likely due to the poor quality of NCEP-GODAS currents, which do not agree with

RAMA observations (Sect. 2). Even though the magnitudes of HYCOM transports are smaller compared to ORAS4, they have consistent effects for both periods (compare red and blue bars). *Qsum* and its time integral show similar decadal reversals for all products, including NCEP-GODAS data (Fig. 8c, d), suggesting that surface heat flux dominates over the meridional heat transport effects in NCEP-GODAS data.

As we shall see below, the increased heat transport out of (into) the NIO during 1993–2003 (2004–2013) is consistent with the spin up (spin down) of the CEC (Fig. 9), which transports more heat out of (into) the NIO for Period I (Period II). The strength of CEC, denoted CEC below, is measured by Sverdrup transport at the equator, which is primarily contributed by the wind stress curl due to zonal wind stress component (Miyama et al. 2003), as shown by Eq. (2) below:

$$CEC(Sv) \approx -\frac{1}{\beta \rho_0} \int_{x_w}^{x_e} \frac{\partial \tau^x}{\partial y} dx, \tag{2}$$
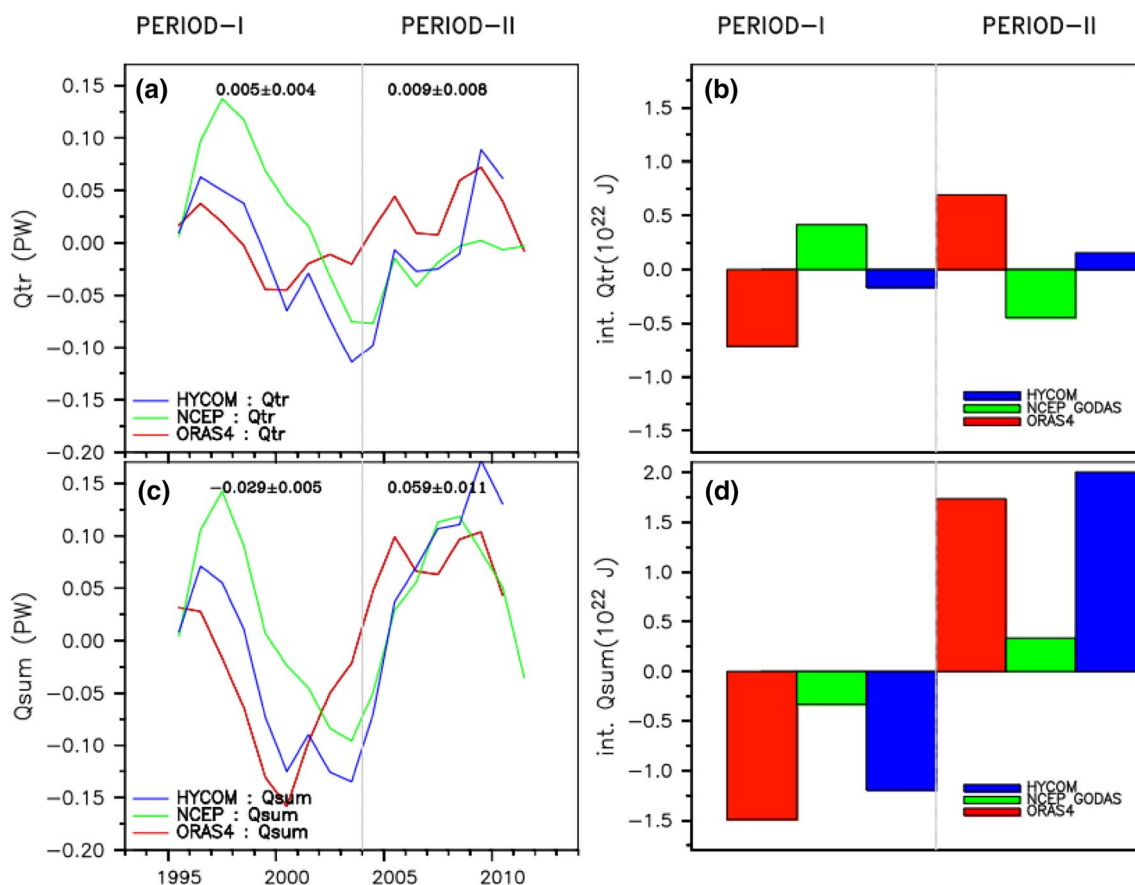
Fig. 8 **a** Zonally integrated heat transport across 5°S in the upper 700 m from ORAS4 data (*red*) compared with that of NCEP-GODAS (*green*) and HYCOM (*blue*); **b** time integrated heat transport (in 10^{22} J) time series of **a**, plotted as *bars* for different products during Period I and Period II; **c** Qsum of ORAS4 (*red*) compared with that of NCEP-GODAS (*green*) and HYCOM (*blue*); **d** time integrated heat transport time series of **c**, plotted as *bars* for different products during Period I and Period II. The mean values of the variables for the Periods I and II are indicated at the *top* of the panels **a**, **c**
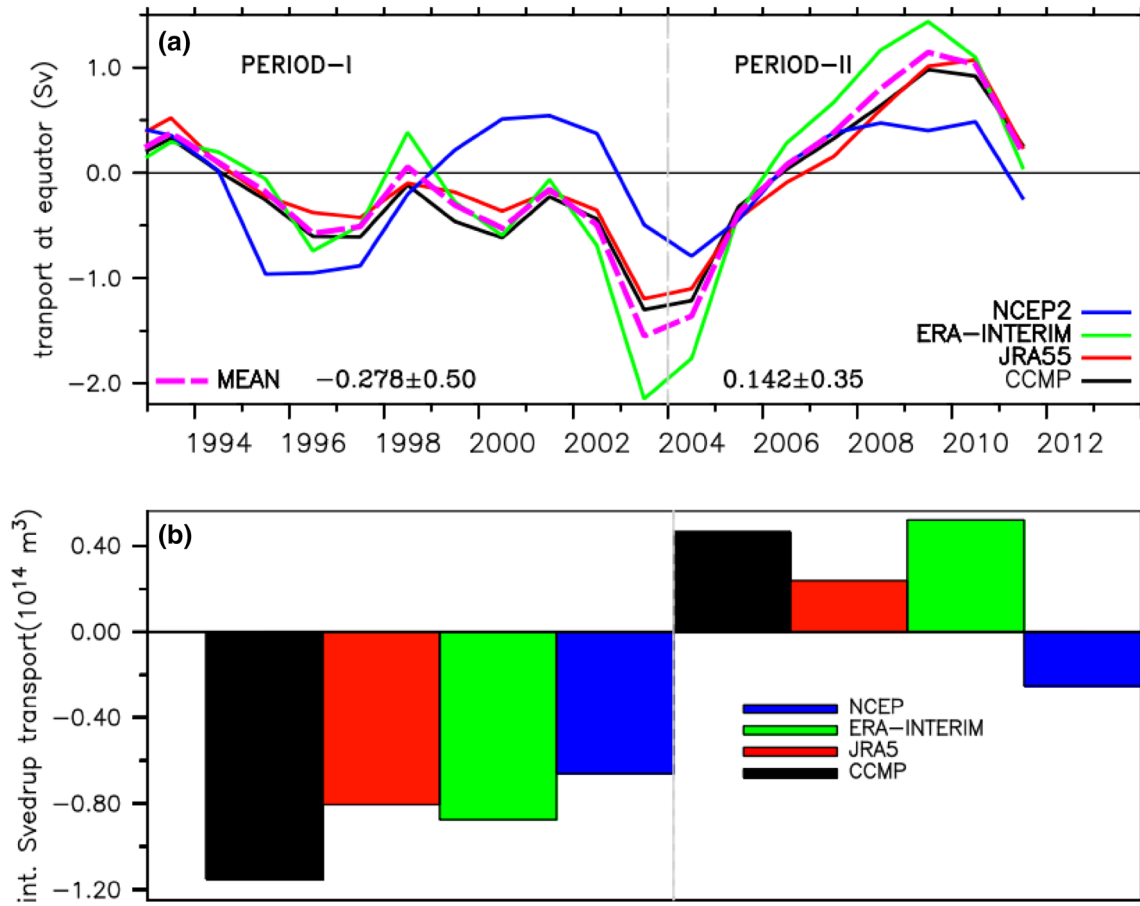
Fig. 9 a Time series of Sverdrup volume transport integrated (from 30°E to 120°E) across Equator from NCEP2 (*blue*), ERA-Interim (*green*) reanalysis, JRA55 (*red*) and CCMP wind (*black*) products for the 1993–2013 period, with linear trend of 1993–2013 removed. It measures the Cross Equatorial Cell (CEC) strength [see Eq. (1a), (1b), (1c) of Sect. 4.1]. *Dashed pink curve* indicates the ensemble mean of all products except NCEP (which is not consistent with other trends). The mean values of transport during the periods I and II are mentioned at the *bottom* of the panel on either side of the line separating the two periods. **b** The time integrated volume transport (in 1014 m3) time series of a, plotted as *bars* for different products during Period I and Period II

where τ^x is the zonal wind stress along the equator, $\beta = \frac{\partial f}{\partial y} = \frac{\partial (2\Omega sin(\phi))}{\partial y} = \frac{2\Omega cos(\phi)}{R}$, Ω is the earth's rotational rate, φ is latitude, R is the Earth's radius, ρ_o is mean density of seawater, and x_e and x_w are the locations of eastern and western boundaries, respectively. The mean strength of the Sverdrup transport at the equator is ~6 Sv and it has reduced by ~2.4 Sv (40%; difference between the values at the beginning and at the ending of mean dashed pink curve) for Period II. This weakened CEC facilitates the reduction in southward heat transport explained above and thus increases the heat content and thermosteric sea level in the NIO. A long term decreasing trend of CEC for the period 1950–1990 was reported earlier (Schoenefeldt and Schott 2006). For Period I (1993–2003), the average anomaly is −0.278 Sv (Fig. 9a), indicating enhanced southward heat transport out of the NIO and reduced heat content and thermosteric sea level over the NIO. The enhanced (Period I)

and diminished (Period II) southward volume transports are more evident to see from Fig. 9b which shows time integrated volume transports computed from various wind products for the Periods I and II. This reversal of volume transport is consistent among the wind products (CCMP, ERA-Interim and JRA55) with NCEP being an exception. NCEP shows a net excessive southward volume transport in both periods similar to the behavior of heat transport observed in NCEP-GODAS. This further augments the observation that the role of meridional transport is less certain in comparison with the role of surface net heat fluxes.

5 Summary and discussions

Satellite and in situ observed monthly-mean sea level anomalies averaged over the Indian Ocean, particularly the NIO, display a distinct decadal reversal near 2003 after

global mean SLR is removed, falling from 1993 to 2003 (Period I) and rising from 2004 to 2013 (Period II; Fig. 1). Consistent with the basin-averaged sea level, the spatial patterns of sea level anomalies also display apparent decadal reversal over the NIO. In the South Indian Ocean south of 5°S and over the tropical Pacific and Atlantic, however, this decadal reversal is absent (Fig. 2), even though SLR in the western tropical Pacific has been intensified during the recent decade. The upper ocean (0–700 m) thermosteric sea level averaged over the NIO agrees well with the satellite observed AVISO sea level, suggesting that thermal expansion of the upper ocean plays an important role in the observed decadal reversal of the total sea level over the NIO. This strong decadal reversal of sea level that occurred in the past two decades appears to be part of the longer-term natural decadal variability (Fig. 3).

Since the NIO basin is only open at 5°S, the change in heat content can only be due to changes in air-sea fluxes or lateral heat transport at 5°S. Figure 10 shows a sketch of the mechanism for the observed decadal sea level reversal near 2003. During Period I, the mean surface heat flux anomaly over the NIO is −0.026 PW based on the ensemble average of Tropflux, ERA-interim and NOCS products, and heat transport anomaly across 5°S is −0.067 PW based on ORAS4 reanalysis (because of its better reliability). The two effects combine to produce a total heat loss of −0.09

PW. For Period II, the NIO gains ~0.015 PW on an average from the surface and ~0.074 PW from heat transport at 5°S, yielding a total heat gain of 0.09 PW. The ~0.074 PW northward heat transport anomaly results from the weakened southward heat transport during Period II, which is associated with the spin-down of the Cross Equatorial Cell. The ~0.015 PW surface heat anomaly is due to the weakened surface turbulent heat loss associated with weakened wind speed over the NIO. During Period I, the southward heat transport across 5°S is enhanced by −0.067 PW due to the spin up of the Cross Equatorial Cell (Fig. 9), exporting more heat out of the NIO. The wind anomalies during Period I are more coherent (resembling annual wind pattern) over the NIO, which drive stronger southward heat and mass transport. During Period II, the wind anomalies are weak and have no apparent large-scale pattern, driving a weaker southward transport. Meanwhile, the increased NIO wind speed increases evaporation and therefore enhances surface turbulent heat loss to the atmosphere from 1993 to 2001 (Fig. 7d). Consequently, it is the NIO heat loss due to the intensified southward heat export and increased surface turbulent heat flux that primarily explains the observed sea level fall from 1993 to 2003 through thermal contraction. The heat gain induces NIO SLR from 2004 to 2013 through thermal expansion. From the HYCOM simulation, it can be shown that the observed sea level reversal in the NIO
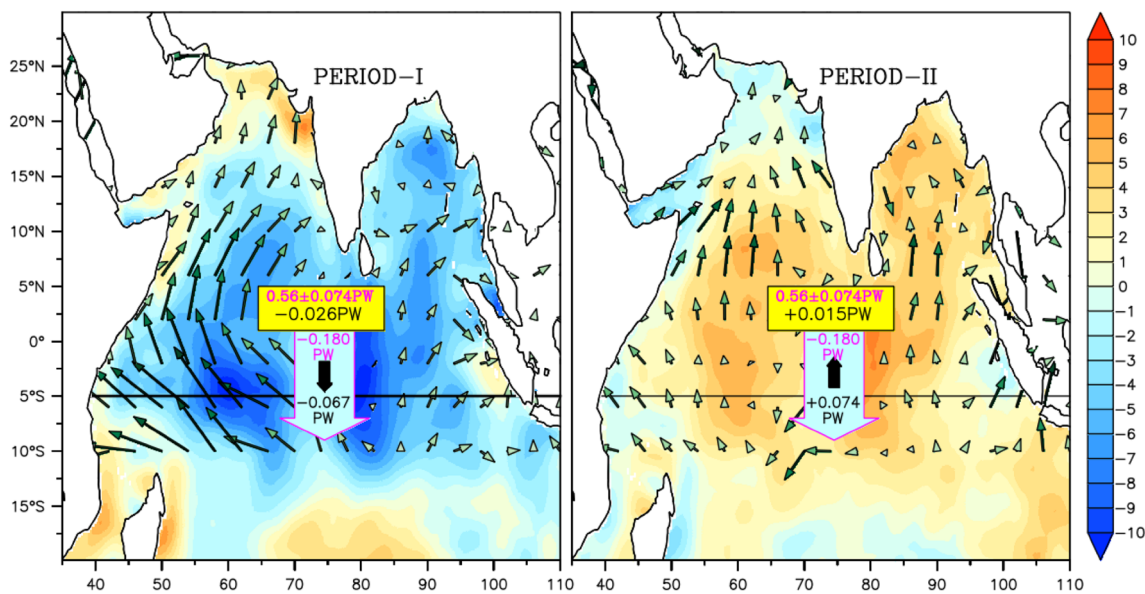

Fig. 10 Schematic diagram summarizing the mechanism of the NIO decadal sea level reversal near 2003: the background color refers to surface net heat flux (W/m^2) anomaly (ensemble average of Tropflux, ERA-interim and NOCS products). The NIO has 0.026 PW surface heat flux deficit in Period I and 0.015 PW surplus in period II, compared to long term mean surface net heat flux (0.56 PW; the consensus value among the four surface net heat flux products mentioned above). See values in the *yellow boxes*. Vectors show wind speed anomalies for each period, which are more coherent (resembling annual wind pattern) over the NIO during Period I and drive stronger southward heat transport. In Period II, surface winds are dispersed, driving a weaker southward heat transport. Mean southward transport is shown in magenta color (−0.18PW; from the more reliable ORAS4 reanalysis data) within the bulk *cyan arrow*. The anomaly values are shown in *black font*. The *dark arrows* within the bulk arrows show the anomalous heat transport across 5°S

is not induced by ITF. Heat advection through ITF may have affected the SIO. The contribution of surface net heat flux to the reversal of thermosteric sea level is robust to cross-dataset differences, whereas the effect of meridional heat transport integrated over periods I and II from NCEP-GODAS data have opposite signs with those of ORAS4 and HYCOM, likely due to the poor quality of NCEP-GODAS currents in the equatorial Indian Ocean (Sect. 2).

The observed decadal reversal of NIO sea level during the recent two decades is a combined effect of meridional heat transport and surface turbulent heat flux (Figs. 6, 7), with both being induced by the decadal changes of sea surface winds. A recent study by Thompson et al. (2016) reports a similar decadal change of NIO sea level. They attributed this reversal to wind driven redistribution of heat caused by weakening and strengthening of Cross Equatorial Cell. While this effect is important, our study also shows an equally important and more coherent effect of surface net heat fluxes across various products. This study offers more quantitative and robust analysis using several datasets and reanalysis products, and assesses the role of ITF in causing the observed reversal, which is not decisively established in Thompson et al. (2016). With the HYCOM experiment where ITF is relaxed, it is clearly shown that ITF has no effect on the NIO observed sea level reversal. Given the profound socioeconomic and environmental impacts of sea level rise, an accurate prediction of the NIO sea level is of paramount need for the surrounding countries. The results of the present study indicate that oceanic processes in the tropical Indian Ocean, such as the meridional heat transport, carry the memory from wind forcing and provide potential predictability for the NIO sea level change. Further investigation should be conducted to establish predictive relationships between surface winds and NIO sea level. In addition, high-quality, real-time ocean surface wind observations are crucial for accurate regional sea level forecasting.

References

Atlas R, Hoffman RN, Ardizzone J, et al (2009) Development of a new cross-calibrated, multi-platform (CCMP) ocean surface wind product. In: AMS 13th Conference on Integrated Observing and Assimilation Systems for Atmosphere, Oceans, and Land Surface (IOAS-AOLS)

Balmaseda MA, Mogensen K, Weaver AT (2013) Evaluation of the ECMWF ocean reanalysis system ORAS4. Q J R Meteorol Soc 139:1132–1161. doi:10.1002/qj.2063

Behringer DW, Xue Y (2004) Evaluation of the global ocean data assimilation system at NCEP: The Pacific Ocean. Eighth Symposium on Integrated Observing and Assimilation Systems for Atmosphere, Oceans, and Land Surface, AMS 84th Annual Meeting, Washington State Convention and Trade Center, Seattle, Washington, pp 11–15

Berry DI, Kent EC (2011) Air-Sea fluxes from ICOADS: the construction of a new gridded dataset with uncertainty estimates. Int J Climatol 31:987–1001. doi:10.1002/joc.2059

Bobba AG (2002) Numerical modelling of salt-water intrusion due to human activities and sea-level change in the Godavari Delta, India. Hydrol Sci J 47:S67–S80. doi:10.1080/02626660209493023

Cazenave A, Cozannet GL (2014) Sea level rise and its coastal impacts: CAZENAVE AND LE COZANNET. Earths Future 2:15–34. doi:10.1002/2013EF000188

Chen G, Han W, Li Y, Wang D, McPhaden M (2015) Seasonal-to-interannual time scale dynamics of the equatorial undercurrent in the Indian Ocean. J Phys Oceanogr 45:1532–1553. doi:10.1175/JPO-D-14-0225.1

Cheng X, Qi Y, Zhou W (2008) Trends of sea level variations in the Indo-Pacific warm pool. Glob Planet Change 63:57–66. doi:10.1016/j.gloplacha.2008.06.001

Church JA, White NJ, Konikow LF, et al (2011) Revisiting the Earth's sea-level and energy budgets from 1961 to 2008: sea-level and energy budgets. Geophys Res Lett doi:10.1029/2011GL048794

Compo GP, Whitaker JS, Sardeshmukh PD, et al (2011) The Twentieth Century Reanalysis Project. Q J R Meteorol Soc 137:1–28. doi:10.1002/qj.776

Dee DP, Uppala SM, Simmons AJ, et al (2011) The ERA-Interim reanalysis: configuration and performance of the data assimilation system. Q J R Meteorol Soc 137:553–597. doi:10.1002/qj.828

Devore J L, Farnum N R, Doi J (2014) Applied statistics for engineers and scientists, 3rd. Brooks/Cole, Stamford, pp 656. ISBN-10: 113311136X

Ducet N, Le Traon P, Reverdin G (2000) Global high-resolution mapping of ocean circulation from TOPEX/Poseidon and ERS-1 and-2. J Geophys Res 105(C8):19477–19498

Ebita A, Kobayashi S, Ota Y, et al (2011) The Japanese 55-year reanalysis "JRA-55": an interim report. SOLA 7:149–152. doi:10.2151/sola.2011-038

Feng M (2004) Multidecadal variations of Fremantle sea level: footprint of climate variability in the tropical Pacific. Geophys Res Lett. doi:10.1029/2004GL019947

Good SA, Martin MJ, Rayner NA (2013) EN4: quality controlled ocean temperature and salinity profiles and monthly objective analyses with uncertainty estimates: THE EN4 DATASET. J Geophys Res Oceans 118:6704–6716. doi:10.1002/2013JC009067

Han W, Meehl GA, Rajagopalan B, et al (2010) Patterns of Indian Ocean sea-level change in a warming climate. Nat Geosci 3:546–550. doi:10.1038/ngeo901

Han W, Meehl GA, Hu A, et al (2014a) Intensification of decadal and multi-decadal sea level variability in the western tropical Pacific during recent decades. Clim Dyn 43:1357–1379. doi:10.1007/s00382-013-1951-1

Han W, Vialard J, McPhaden MJ, et al (2014b) Indian Ocean decadal variability: a review. Bull Am Meteorol Soc 95:1679–1703.

Han W, Meehl GA, Stammer D, Hu A, Hamlington B, Kenigson J, Palanisamy H, Thompson P (2017) Spatial patterns of sea level variability associated with natural internal climate modes. Surv Geophys 38(1):217-250

Ishii M, Kimoto M, Sakamoto K, Iwasaki S-I (2006) Steric sea level changes estimated from historical ocean subsurface temperature and salinity analyses. J Oceanogr 62:155–170

Johnson GC, Chambers DP (2013) Ocean bottom pressure seasonal cycles and decadal trends from GRACE Release-05: Ocean circulation implications: grace seasonal cycles and decadal trends. J Geophys Res Oceans 118:4228–4240. doi:10.1002/jgrc.20307

Kanamitsu M, Ebisuzaki W, Woollen J, et al (2002) NCEP–DOE AMIP-II Reanalysis (R-2). Bull Am Meteorol Soc 83:1631–1643. doi:10.1175/BAMS-83-11-1631

Karim M, Mimura N (2008) Impacts of climate change and sea-level rise on cyclonic storm surge floods in Bangladesh. Glob Environ Change 18:490–500. doi:10.1016/j.gloenvcha.2008.05.002

Lee T (2004) Decadal weakening of the shallow overturning circulation in the South Indian Ocean. Geophys Res Lett. doi:10.1029/2004GL020884

Lee T, McPhaden MJ (2008) Decadal phase change in large-scale sea level and winds in the Indo-Pacific region at the end of the 20th century. Geophys Res Lett. doi:10.1029/2007GL032419

Lee, S. K., W. Park, M.O. Baringer, A.L. Gordon, B. Huber and Y. Liu (2015) Pacific origin of the abrupt increase in Indian Ocean heat content during the warming hiatus. Nat Geosci 8, 445–449.

Levitus S, Antonov JI, Boyer TP, et al (2012) World ocean heat content and thermosteric sea level change (0–2000 m), 1955–2010: WORLD OCEAN HEAT CONTENT. Geophys Res Lett 39: doi:10.1029/2012GL051106

Li Y, Han W (2015) Decadal sea level variations in the Indian Ocean investigated with HYCOM: roles of climate modes, ocean internal variability, and stochastic wind forcing. J Clim 28:9143–9165. doi:10.1175/jcli-d-15-0252.1

Llovel W, Lee T (2015) Importance and origin of halosteric contribution to sea level change in the southeast Indian Ocean during 2005–2013: Halosteric sea level change. Geophys Res Lett 42:1148–1157. doi:10.1002/2014GL062611

Madec G (2015) NEMO ocean engine. Note du Pole de modélisation de l' Institut Pierre-Simon Laplace, Paris, France, 27, 401 pp, hdl:10013/epic.46840.d001

McPhaden MJ, Meyers G, Ando K, Masumoto Y, Murty VSN, Ravichandran M, Syamsudin F, Vialard J, Yu L, Yu W (2009) RAMA: the research moored array for African–Asian–Australian monsoon analysis and prediction. Bull Am Meteorol Soc 90:459–480

Melini D, Piersanti A (2006) Impact of global seismicity on sea level change assessment. J Geophys Res. doi:10.1029/2004JB003476

Merrifield MA (2011) A shift in western tropical pacific sea level trends during the 1990s. J Clim 24:4126–4138. doi:10.1175/2011JCLI3932.1

Merrifield MA, Maltrud ME (2011) Regional sea level trends due to a pacific trade wind intensification: sea level and pacific trade winds. Geophys Res Lett. doi:10.1029/2011GL049576

Milne GA, Gehrels WR, Hughes CW, Tamisiea ME (2009) Identifying the causes of sea-level change. Nat Geosci 2:471–478. doi:10.1038/ngeo544

Mitrovica JX, Tamisiea ME, Davis JL, Milne GA (2001) Recent mass balance of polar ice sheets inferred from patterns of global sea-level change. Nature 409:1026–1029

Miyama T, McCreary JP, Jensen TG, et al (2003) Structure and dynamics of the Indian-Ocean cross-equatorial cell. Deep Sea Res Part II Top Stud Oceanogr 50:2023–2047. doi:10.1016/S0967-0645(03)00044-4

Mogensen K, Alonso Balmaseda M, Weaver A (2012) The NEMO-VAR ocean data assimilation system as implemented in the ECMWF ocean analysis for System 4. European Centre for Medium-Range Weather Forecasts

Nerem RS, Chambers DP, Choe C, Mitchum GT (2010) Estimating mean sea level change from the TOPEX and jason altimeter missions. Mar Geod 33:435–446. doi:10.1080/01490419.2010.491031

Nidheesh AG, Lengaigne M, Vialard J, et al (2013) Decadal and long-term sea level variability in the tropical Indo-Pacific Ocean. Clim Dyn 41:381–402. doi:10.1007/s00382-012-1463-4

Nieves V, Willis JK, Patzert WC (2015) Recent hiatus caused by decadal shift in Indo-Pacific heating. Science 349:532–535

Praveen Kumar B, Vialard J, Lengaigne M, et al (2012) TropFlux: air-sea fluxes for the global tropical oceans—description and evaluation. Clim Dyn 38:1521–1543. doi:10.1007/s00382-011-1115-0

Quinn KJ, Ponte RM (2010) Uncertainty in ocean mass trends from GRACE. Geophys J Int doi:10.1111/j.1365-246X.2010.04508.x

Ravichandran M, BehringerD, Sivareddy S et al (2013) Evaluation of the global ocean data assimilation system at INCOIS: the tropical Indian Ocean. Ocean Model 69:123–135. doi:10.1016/j.ocemod.2013.05.003

Rignot E, Velicogna I, van den Broeke MR, et al (2011) Acceleration of the contribution of the Greenland and Antarctic ice sheets to sea level rise: acceleration of ice sheet loss. Geophys Res Lett. doi:10.1029/2011GL046583

Roemmich D, Gilson J (2009) The 2004–2008 mean and annual cycle of temperature, salinity, and steric height in the global ocean from the Argo Program. Prog Oceanogr 82:81–100. doi:10.1016/j.pocean.2009.03.004

Rowley RJ, Kostelnick JC, Braaten D et al (2007) Risk of rising sea level to population and land area. Eos. Trans Am Geophys Union 88:105–107

Santer BD, Boyle JS, Hnilo JJ et al (2000) Statistical significance of trends and trend differences in layer-average atmospheric temperature time series. J Geophys Res 105:7337–7356

Schoenefeldt R, Schott FA (2006) Decadal variability of the Indian Ocean cross-equatorial exchange in SODA. Geophys Res Lett. doi:10.1029/2006GL025891

Schott FA, McCreary JP (2001) The monsoon circulation of the Indian Ocean. Prog Oceanogr 51:1–123.

Schott FA, McCreary JP, Johnson GC (2004) Shallow overturning circulations of the tropical-subtropical oceans. In: Wang C, Xie S-P, Carton JA (eds) Earth climate: the ocean-atmosphere interaction, Geophys. Monogr. Ser., vol. 147. AGU, Washington, D. C, pp 261–304

Schott FA, Xie S-P, McCreary JP (2009) Indian Ocean circulation and climate variability. Rev Geophys. doi:10.1029/2007RG000245

Sivareddy S (2015) A study on global ocean analysis from an ocean data assimilation system and its sensitivity to observations and forcing fields. Ph.D. thesis, Andhra University. (Available online at http://www.incois.gov.in/documents/PhDThesis_Sivareddy.pdf)

Slangen AB, Lenaerts JT (2016) The sea level response to ice sheet freshwater forcing in the Community Earth System Model. Environ Res Lett 11:104002

Sprintall J, Wijffels SE, Molcard R, Jaya I (2009) Direct estimates of the Indonesian Throughflow entering the Indian Ocean: 2004–2006. J Geophys Res. doi:10.1029/2008JC005257

Stammer D, Hüttemann S (2008) Response of regional sea level to atmospheric pressure loading in a climate change scenario. J Clim 21:2093–2101

Stammer D, Agarwal N, Herrmann P, Köhl A, Mechoso CR (2011) Response of a coupled ocean–atmosphere model to Greenland ice melting. Surv Geophys 32(4-5):621

Stammer D, Cazenave A, Ponte RM, Tamisiea ME (2013) Causes for contemporary regional sea level changes. Annu Rev Mar Sci 5:21–46. doi:10.1146/annurev-marine-121211-17240

Thompson, P. R., et al. (2016) Forcing of recent decadal variability in the Equatorial and North Indian Ocean. J Geophys Res Oceans 121(9): 6762–6778

Timmermann A, McGregor S, Jin F-F (2010) Wind effects on past and future regional sea level trends in the southern indo-pacific. J Clim 23:4429–4437. doi:10.1175/2010JCLI3519.1

Trenary LL, Han W (2012) Intraseasonal-to-interannual variability of south indian ocean sea level and thermocline: remote versus local forcing. J PhysOceanogr 42:602–627. doi:10.1175/JPO-D-11-084.1

Unnikrishnan AS, Nidheesh AG, Lengaigne M (2015) Sea level rise trends off the Indian coasts during the last two decades. Curr Sci 108(5): 966–971

Vialard J (2015) Ocean science: Hiatus heat in the Indian Ocean. Nat Geosci 8(6): 423–424

Vidard A, Balmaseda M, Anderson D (2009) Assimilation of altimeter data in the ECMWF ocean analysis system 3. Mon. Weather Rev Am Meteorol Soc 137(4):1393–1408

Werner AD, Simmons CT (2009) Impact of sea-level rise on sea water intrusion in coastal aquifers. Ground Water 47:197–204. doi:10.1111/j.1745-6584.2008.00535.x

Yu L, Weller R (2007) Objectively analyzed air–sea heat fluxes for the global ice-free Oceans (1981–2005). Bull Am Meteorol Soc 88: 527–539. doi:10.1175/BAMS-88-4-527